International Journal of Solids and Structures 50 (2013) 1342–1353

Contents lists available at SciVerse ScienceDirect

International Journal of Solids and Structures

journal homepage: www.elsevier.com/locate/ijsolstr

Analysis and optimal design of layered composites with high stiffness and high damping

Julien Meaud [a,*], Trisha Sain [b], Gregory M. Hulbert [a], Anthony M. Waas [a,b]

[a] Department of Mechanical Engineering, University of Michigan, Ann Arbor, United States
[b] Department of Aerospace Engineering, University of Michigan, Ann Arbor, United States

ARTICLE INFO

Article history:
Received 20 October 2012
Received in revised form 27 December 2012
Available online 24 January 2013

Keywords:
Composite materials
Optimization
Viscoelastic
Damping

ABSTRACT

In this paper we investigate the design of composite materials with simultaneously high stiffness and high damping. We consider layered composite materials with parallel plane layers made of a stiff constituent and a lossy polymer. We analyze the response of these composites to a dynamic load with an arbitrary direction. Using the viscoelastic correspondence principle and linear frequency domain viscoelastic models, we derive an expression for the effective complex modulus of layered composites of infinite size at infinitesimal strains. The dependence of the effective dynamic modulus and loss factor on the geometrical parameters and on the tensile and bulk loss factors of the lossy constituent is analyzed. Moreover we determine the magnitude of the strains in the lossy constituent and demonstrate that the combination of high stiffness and high damping of these composites is due to the high normal and/or shear strains in the lossy material. We use nonlinear constrained optimization to design layered composites with simultaneously high stiffness and high damping while constraining the strains in the polymer. To determine the range of validity of the linear viscoelastic model, simulations using finite deformations models are compared to the theoretical results. Finally, we compute the effective properties of composites of finite size using finite element methods and determine the minimum size required to approach the formulae derived for composites of infinite size.

1. Introduction

The analysis and design of multifunctional materials is a topic of active research (Cadman et al., 2012). The design of composite materials with competing attributes have been explored using mainly multiobjective topology optimization techniques. Examples of composite properties that were optimized include stiffness and permeability (Guest and Prevost, 2006), transport of heat and electricity (Torquato et al., 2002), and stiffness and resistance to heat (de Kruijf et al., 2007). In this work we derive an analytical model and use numerical optimization to design a class of composite materials with simultaneously high stiffness and high damping.

As discussed in Lakes (2009), materials with both high damping and stiffness would be useful in structural applications. However, materials with high damping (such as high loss elastomers) tend to be soft (Lakes, 2009; Ashby, 1989). Viscoelastic composites with a stiff constituent and a lossy, soft constituent might achieve a combination of high stiffness and high damping. The design of composite topologies with high stiffness and/or damping have been investigated before using analytical and computational methods. Lakes and coworkers investigated various topologies with high stiffness and damping (Chen and Lakes, 1993; Kim et al., 2002; Lakes, 2002). Chen and Lakes derived formulae for the Reuss and Voigt topologies and composites with spherical particulate inclusions (Chen and Lakes, 1993). Kim et al. (2002) used computational homogenization to determine the effective dynamic properties of SiC–InSn particulate reinforced composites. Lakes (2002) showed that hierarchical particulate morphologies can achieve high stiffness and damping. Other theoretical studies include the design of composites with optimal damping and/or stiffness using topology optimization by Yi et al. (2000). Patel et al. used the finite element method to design viscoelastic composite materials with high damping over a wide frequency range (Patel et al., 2007). Prasad and Diaz designed viscoelastic composites that include a negative stiffness constituent and with a target effective viscoelastic tensor (Prasad and Diaz, 2009) using topology optimization and inverse homogenization. In a recent study we investigated using finite element methods the effective stiffness and damping of composites with wavy layers (Sain et al., in press).

In this paper we focus on layered composites with parallel plane layers of two constituents. Layered composites are of interest because they are simple to manufacture. Neglecting the Poisson effects, Chen and Lakes (1993) derived formulae for the effective dynamic properties of layered composites loaded in the layer direction (Voigt topology) and perpendicular to the layer direction

* Corresponding author. Tel.: +1 7342721069.
E-mail address: jmeaud@umich.edu (J. Meaud).

0020-7683/$ - see front matter © 2013 Elsevier Ltd. All rights reserved.
http://dx.doi.org/10.1016/j.ijsolstr.2013.01.014

(Reuss topology). The Reuss topology was found to combine high stiffness with high damping. Brodt and Lakes measured the effective dynamic properties in bending of Reuss beams (Brodt and Lakes, 1995). Liu *et al.* derived formulae for the effective elastic moduli of Reuss and Voigt composites taking into account Poisson effects (Liu et al., 2009). Applying the correspondence principle to those equations, we derived equations for the effective dynamic properties of Reuss and Voigt composites (Meaud and Hulbert, in press). We demonstrated that the loss factor of a Reuss composite is significantly lower while its effective dynamic modulus is much higher when Poisson effects are taken into account, compared to the formula derived by Chen and Lakes (Meaud and Hulbert, in press). We also showed that the effective properties of Reuss composites of finite size are very sensitive to the ratio of the in plane dimensions to the layer thickness.

In this paper we derive the effective dynamic properties of layered composites in response to a uniaxial load in an arbitrary direction at infinitesimal strains. Many engineering structures are primarily subject to uniaxial loads. However, while materials and structures with high stiffness and high damping under bending or shear deformation exist (such as constrained damping layer for beam bending), materials with high stiffness and damping under uniaxial loads are less common. We demonstrate that the layered composites can attain simultaneously high stiffness and high damping under uniaxial loads depending on the orientation of the layers and on the volume fractions of the constituents. We evaluate the strains in the polymer and show that the high values of stiffness and damping of these layered composites are due to large strains in the polymer. We present results from optimization to maximize damping and stiffness of the composites while constraining the maximum allowable strains in the polymer. Theoretical results are compared to simulations using finite strain viscoelastic models to establish the maximum macroscopic strain amplitudes for which the linear viscoelastic theory approximates the finite deformation theory. Following our previous findings for Reuss composites of finite size (Meaud and Hulbert, in press), we also compute the effective properties of layered composites of finite size and determine the minimum number of layers and minimum height to width ratio required to approach the formulae derived for composites of infinite size.

2. Effective dynamic properties of layered composites

2.1. Notations and assumptions

We consider a layered composite with layers of a stiff material, material A, and a soft and lossy material, material B (Fig. 1). Let x and y be the material principal directions and z the direction perpendicular to the layers. Let (X, Y, Z) be a another set of axis, representing a fixed Cartesian, Newtonian reference frame, such that $Y = y$ and the angle between x and X and between z and Z is θ. We derive the effective properties of the composite when loaded in the X direction. Using this notation, θ is the angle between the layer direction and the load direction and the configuration $\theta = 0°$(respectively $\theta = 90°$) corresponds to the Voigt topology (respectively Reuss topology).

For the derivations presented in this section, the composites are assumed to have infinite size. Moreover perfect bonding is assumed between the layers. As in our previous work (Meaud and Hulbert, in press), we modeled material A and B as linear viscoelastic materials in the frequency domain using complex notation (Lakes, 2009; Christensen, 2003). A complex number is denoted by *, i is the imaginary unit number, *Re* denotes the real part and *Im* the imaginary part. The frequency of the load is assumed to be sufficiently low such that inertial effects can be ignored. In each

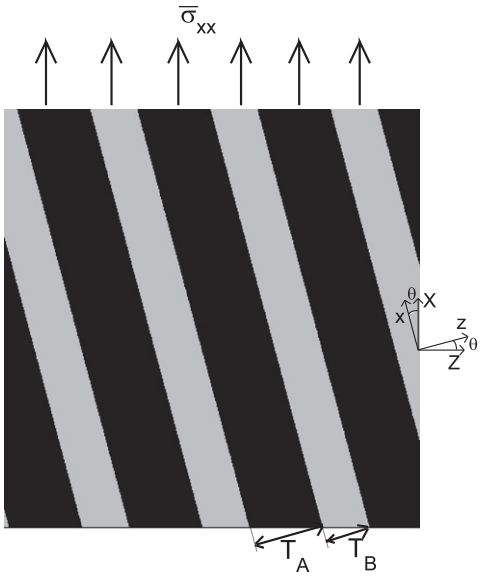

Fig. 1. Layered composites with layers of material A, of thickness T_A, and of material B, of thickness T_B. The x axis corresponds to the layer, the y axis is out of plane and the z axis is perpendicular to the layers. The composites are loaded in a direction X, where the angle between x and X is θ.

layer, the values of the stress and strain components are independent of the position and are denoted by the subscript A or B depending on the material of the layer. An overbar denotes the macroscopic value of stress and strain component. In response to a dynamic load, the relationship between the complex valued normal stress, $\bar{\sigma}^*_{XX}$, and the complex-valued normal strain, $\bar{\epsilon}^*_{XX}$, is:

$$\bar{\sigma}^*_{XX} = E^*_{XX}\bar{\epsilon}^*_{XX} \tag{1}$$

where E^*_{XX} is the effective complex Young's modulus in the X direction. The dynamic modulus, $|E^*_{XX}|$, and loss factor, η_{XX}, are given by:

$$|E^*_{XX}| = \sqrt{Re(E^*_{XX})^2 + Im(E^*_{XX})^2} \tag{2}$$

$$\eta_{XX} = \frac{Im(E^*_{XX})}{Re(E^*_{XX})} \tag{3}$$

$|E^*_{XX}|$ is a measure of the stiffness of the material in response to a uniaxial dynamic load and η_{XX} is a measure of its damping capacity.

2.2. Derivations of the effective properties

$\bar{\sigma}^*_{XX}$ is the only non-zero macroscopic component of stress in the (X, Y, Z) coordinate system. Therefore, in the (x, y, z) coordinate system, $\bar{\sigma}^*_{yy} = \bar{\sigma}^*_{yz} = \bar{\sigma}^*_{xy} = 0$ while in a general case $\bar{\sigma}^*_{xx} \neq 0$, $\bar{\sigma}^*_{zz} \neq 0$ and $\bar{\sigma}^*_{xz} \neq 0$. The relation between the strain vector $\bar{\boldsymbol{\epsilon}}^*_{(x,y,z)} = [\bar{\epsilon}^*_{xx}, \bar{\epsilon}^*_{yy}, \bar{\epsilon}^*_{zz}, \bar{\gamma}^*_{yz}, \bar{\gamma}^*_{zx}, \bar{\gamma}^*_{xy}]^T$ and the stress vector $\bar{\boldsymbol{\sigma}}^*_{(x,y,z)} = [\bar{\sigma}^*_{xx}, \bar{\sigma}^*_{yy}, \bar{\sigma}^*_{zz}, \bar{\tau}^*_{yz}, \bar{\tau}^*_{zx}, \bar{\tau}^*_{xy}]^T$ is given by:

$$\bar{\boldsymbol{\epsilon}}^*_{(x,y,z)} = [\mathbf{s}^*]\bar{\boldsymbol{\sigma}}^*_{(x,y,z)} \tag{4}$$

were $[\mathbf{s}^*]$ is the compliance matrix:

$$[\mathbf{s}^*] = \begin{pmatrix} s^*_{11} & s^*_{12} & s^*_{13} & 0 & 0 & 0 \\ & s^*_{11} & s^*_{13} & 0 & 0 & 0 \\ & & s^*_{33} & 0 & 0 & 0 \\ sym & & & s^*_{55} & 0 & 0 \\ & & & 0 & s^*_{55} & 0 \\ & & & & & s^*_{66} \end{pmatrix} \tag{5}$$

An expression for s^*_{ij} can be found by applying the viscoelastic correspondence principle to the equations derived by Liu et al. (2009). In particular,

$$s^*_{11} = \frac{1}{E^*_{11}} = \frac{1}{E^*_{eff}\big|_{Voigt}} \tag{6}$$

$$s^*_{33} = \frac{1}{E^*_{33}} = \frac{1}{E^*_{eff}\big|_{Reuss}} \tag{7}$$

where $E^*_{eff}\big|_{Voigt}$ (respectively $E^*_{eff}\big|_{Reuss}$) is the effective Young's modulus of the Voigt topology (respectively Reuss topology) and is given in Meaud and Hulbert (in press). Applying the viscoelastic correspondence principle to Eqs. (22), (30) and (35) in Liu et al. (2009),

$$s^*_{13} = \frac{\Phi_A v^*_A + \Phi_B v^*_B - v^*_A v^*_B}{\Phi_A v^*_B E^*_A + \Phi_B v^*_A E^*_B - \Phi_A E^*_A - \Phi_B E^*_B} \tag{8}$$

$$s^*_{12} = \frac{\Phi_A v^*_A E^*_A + \Phi_B v^*_B E^*_B - \Phi_A v^*_A v^{*2}_B E^*_A - \Phi_B v^*_B v^{*2}_A E^*_B}{\left(\Phi_A v^*_B E^*_A + \Phi_B v^*_A E^*_B\right)^2 - \left(\Phi_A E^*_A + \Phi_B E^*_B\right)^2} \tag{9}$$

$$s^*_{55} = \frac{1}{G^*_{eff}\big|_{xz}} \tag{10}$$

where Φ_A (respectively Φ_B) is the volume fraction of material A (respectively B), v^*_A (respectively v^*_B) is the complex Poisson's ratio of material A (respectively B), E^*_A (respectively E^*_B) is the complex Young's modulus of material A (respectively B) and $G^*_{eff}\big|_{xz}$ is the effective complex shear modulus and is given by:

$$G^*_{eff}\big|_{xz} = \frac{1}{\frac{\Phi_A}{G^*_A} + \frac{\Phi_B}{G^*_B}} \tag{11}$$

where G^*_A (respectively G^*_B) is the complex shear modulus of material A (respectively B).

The relationship between the strain vector, $\bar{\boldsymbol{\epsilon}}^*_{(X,Y,Z)} = [\bar{\epsilon}^*_{XX}, \bar{\epsilon}^*_{YY}, \bar{\epsilon}^*_{ZZ}, \bar{\gamma}^*_{YZ}, \bar{\gamma}^*_{ZX}, \bar{\epsilon}^*_{XY}]^T$ and the stress vector $\bar{\boldsymbol{\sigma}}^*_{(X,Y,Z)} = [\bar{\sigma}^*_{XX}, \bar{\sigma}^*_{YY}, \bar{\sigma}^*_{ZZ}, \bar{\tau}^*_{YZ}, \bar{\tau}^*_{ZX}, \bar{\tau}^*_{XY}]^T$ is :

$$\bar{\boldsymbol{\epsilon}}^*_{(X,Y,Z)} = [\mathbf{S}^*]\bar{\boldsymbol{\sigma}}^*_{(X,Y,Z)} \tag{12}$$

where the compliance matrix $[\mathbf{S}^*]$ is given by:

$$[\mathbf{S}^*] = \begin{pmatrix} S^*_{11} & S^*_{12} & S^*_{13} & S^*_{14} & S^*_{15} & S^*_{16} \\ & S^*_{22} & S^*_{23} & S^*_{24} & S^*_{25} & S^*_{26} \\ & & S^*_{33} & S^*_{34} & S^*_{35} & S^*_{36} \\ sym & & & S^*_{44} & 0 & 0 \\ & & & 0 & S^*_{55} & 0 \\ & & & & & S^*_{66} \end{pmatrix} = [\mathbf{R}]^{\mathbf{T}}[\mathbf{s}^*][\mathbf{R}] \tag{13}$$

in which $[\mathbf{R}]$ is expressed as:

$$[\mathbf{R}] = \begin{pmatrix} \cos^2\theta & 0 & \sin^2\theta & 0 & -\sin 2\theta & 0 \\ 0 & 1 & 0 & 0 & 0 & 0 \\ \sin^2\theta & 0 & \cos^2\theta & 0 & \sin 2\theta & 0 \\ 0 & 0 & 0 & \cos\theta & 0 & \sin\theta \\ \sin\theta\cos\theta & 0 & -\sin\theta\cos\theta & 0 & \cos^2\theta - \sin^2\theta & 0 \\ 0 & 0 & 0 & -\sin\theta & 0 & \cos\theta \end{pmatrix} \tag{14}$$

Therefore the effective complex modulus in the X direction is:

$$E^*_{XX} = \frac{1}{S^*_{11}} = \left[\frac{\cos^4\theta}{E^*_{eff}\big|_{Voigt}} + \frac{\sin^4\theta}{E^*_{eff}\big|_{Reuss}} + \frac{\cos^2\theta\sin^2\theta}{G^*_{eff}\big|_{xz}} + 2s^*_{13}\cos^2\theta\sin^2\theta\right]^{-1} \tag{15}$$

Eq. (15) shows that the effective complex Young's modulus is a function of the volume fraction of material A, Φ_A (because $E^*_{eff}\big|_{Voigt}$, $E^*_{eff}\big|_{Reuss}$, $G^*_{eff}\big|_{xz}$ and s^*_{13} depends on Φ_A) and of the angle θ.

2.3. Material parameters

As discussed in Meaud and Hulbert (in press), a linear viscoelastic material is characterized at a radian frequency ω by the values of its dynamic Young's modulus, $|E^*|$, the real part of the Poisson's ratio, v', the tensile loss factor, η_E, and the bulk loss factor, η_K. For the analysis herein, we consider material A to have the following properties: $|E^*_A| = 200$ GPa, $v'_A = 0.3$ and $\eta_{EA} = \eta_{KA} = 0.001$. For material B, we use $|E^*_B| = 20$ MPa, $v'_B = 0.45$, $\eta_{EB} = 1.0$ and $\eta_{KB} = \sqrt{1-2v'_B}$. The properties of material A correspond to steel; the properties of material B correspond to a high loss elastomer. The choice of the bulk of the loss factor of material B is motivated by our analysis in Meaud and Hulbert (in press).

2.4. Stiffness, damping and stiffness-loss map as a function of Φ_A

Fig. 2 presents the variations in the dynamic modulus, loss factor and stiffness-loss map, computed numerically using Eqs. (2), (3) and (15), as a function of Φ_A and θ. At any given volume fraction, the Voigt topology has the highest stiffness among the plotted configurations. However the Reuss topology does not have the lowest stiffness, as $\theta = 45°$ is predicted to have a lower stiffness than $\theta = 90°$. This result is due to the Poisson effects that significantly increase the stiffness of the Reuss topology, as discussed by Liu et al. (2009). Interestingly, there is an increase of several orders of magnitude in $|E^*_{XX}|$ when Φ_A approaches 100%, and $\theta > 1°$.

In the plot of the loss factor as a function of Φ_A shown in Fig. 2b, the Voigt topology has the lowest damping among the plotted configurations. The $\theta = 45°$ configuration provides the highest damping at low volume fractions (less than about 1%) while $\theta = 10°$ has the highest damping at higher volume fractions. A nonmonotonic response is observed for $\theta = 1°$, $10°$ and $45°$.

The stiffness-loss map (a plot of the effective dynamic modulus as a function of the loss factor) is shown in Fig. 2c. Points on each line corresponds to different values of Φ_A. The stiffness-loss map for the Voigt and Reuss topology (with Poisson effects) were described in Meaud and Hulbert (in press). The configurations $\theta = 1°$ and $10°$ behave like the Voigt topology at low volume fractions (high stiffness, low damping) and like the Reuss topology at high volume fractions. The response for the $\theta = 45°$ configuration is almost a vertical line at low values of Φ_A, which implies that $|E^*_{XX}|$ increases without any significant decrease in η_{XX} as Φ_A is increased. It is clear from this figure that the configuration $\theta = 10°$ best combines high stiffness and high damping (for high values of Φ_A), since the corresponding curve approaches the top right hand corner of the figure. In particular, this topology is significantly better than the Reuss topology (with Poisson effects). This unexpected result is due to the axial-shear coupling that is induced by the angled (with respect to the load) layers.

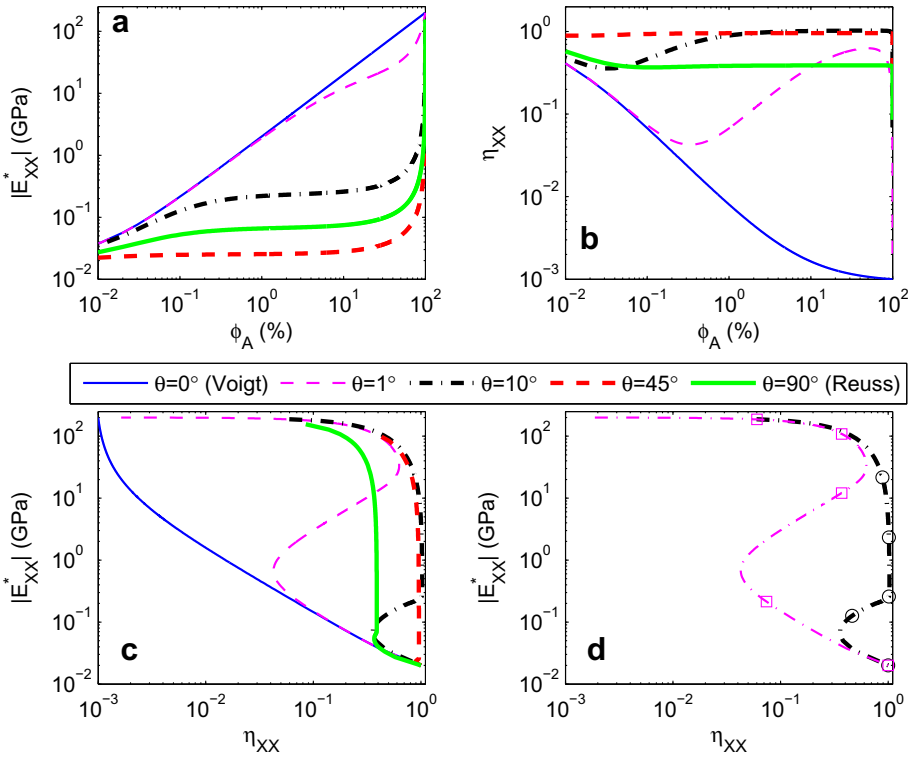

Fig. 2. Dynamic modulus, $|E^*_{XX}|$, and loss factor, η_{XX}, of layered composites. a. Dynamic modulus as a function of the volume fraction of material A, Φ_A. b. Loss factor as a function of Φ_A. c. and d. Stiffness-loss map for different values of θ. In d., squares and circles correspond to Φ_A = 0%, 0.1%, 10%, 90% and 99%.

2.5. Dependence of the loss factor on the tensile loss factor and bulk loss factor of the lossy material

We found in Meaud and Hulbert (in press) that the effective loss factor of the Reuss composite is highly dependent on the bulk loss factor of the lossy constituent. Such a dependency is not desirable since the bulk loss factor of most materials tends to be low (Pritz, 2009) and is rarely measured. We analyzed the dependency of the effective loss factor of layered composites on the tensile and bulk loss factors of material B as shown in Fig. 3. For the results given in Fig. 3a, $\eta_{EB} = 1$ and $0 \leqslant \eta_{KB} \leqslant 1$. In contrast to the case of the Reuss topology, the loss factor obtained for $\theta = 0°$, 10° and 45° is nearly independent of η_{KB}. In Fig. 3b, $\eta_{KB} = 1$ and $0 \leqslant \eta_{EB} \leqslant 1$. The loss factors of the Reuss and Voigt composites are not very sensitive to η_{EB}. In contrast, the effective loss factor obtained for $\theta = 10°$ and 45° varies linearly with η_{EB}, with a slope almost equal to 1.

3. Strains in the soft and lossy constituent

High levels of damping and stiffness can be seen in these composites because of the nonaffine deformation (Chen and Lakes, 1993). We show below that the strains in material B are much higher than the macroscopic strain $\bar{\epsilon}^*_{ZZ}$ for the configurations that have high stiffness and high damping. We derive the expression for the strains in material B in the (x, y, z) coordinate system in order to better understand the mechanisms of damping in these layered composites. In response to a macroscopic normal stress, $\bar{\sigma}^*_{XX}$, the macroscopic stress components in the (x, y, z) coordinate systems are:

$$\begin{pmatrix} \bar{\sigma}^*_{xx} \\ \bar{\sigma}^*_{zz} \\ \bar{\tau}^*_{xz} \end{pmatrix} = \begin{pmatrix} \cos^2\theta \\ \sin^2\theta \\ \sin\theta\cos\theta \end{pmatrix} \bar{\sigma}^*_{XX} \tag{16}$$

3.1. Normal strains

The *xx* and *yy* components of strain in material B are the same as the macroscopic components and are given by:

$$\epsilon^*_{xx}|_B = s^*_{11}\bar{\sigma}^*_{xx} + s^*_{13}\bar{\sigma}^*_{zz} = \left[\frac{\cos^2\theta}{E^*_{eff}\big|_{Voigt}} + s^*_{13}\sin^2\theta\right] E^*_{XX}\bar{\epsilon}^*_{XX} \tag{17}$$

and

$$\epsilon^*_{yy}\Big|_B = s^*_{21}\bar{\sigma}^*_{xx} + s^*_{23}\bar{\sigma}^*_{zz} = \left[s^*_{12}\cos^2\theta + s^*_{13}\sin^2\theta\right] E^*_{XX}\bar{\epsilon}^*_{XX} \tag{18}$$

The *zz* component of strain in the polymer can be decomposed into the term due to stress $\bar{\sigma}^*_{xx}$, $\epsilon^*_{zz}|_{B,\bar{\sigma}^*_{xx}}$, and the term due to the stress $\bar{\sigma}^*_{zz}$, $\epsilon^*_{zz}|_{B,\bar{\sigma}^*_{zz}}$:

$$\epsilon^*_{zz}|_B = \epsilon^*_{zz}|_{B,\bar{\sigma}^*_{xx}} + \epsilon^*_{zz}|_{B,\bar{\sigma}^*_{zz}} \tag{19}$$

In response to stress $\bar{\sigma}_{xx}$, $\sigma^*_{zz}|_B = 0$, $\epsilon^*_{xx}|_{B,\bar{\sigma}^*_{xx}} = \bar{\epsilon}^*_{xx}|_{\bar{\sigma}^*_{xx}}$ and $\epsilon^*_{yy}\Big|_{B,\bar{\sigma}^*_{xx}} = \bar{\epsilon}^*_{yy}\Big|_{\bar{\sigma}^*_{xx}}$ so that:

$$\epsilon^*_{zz}|_{B,\bar{\sigma}^*_{xx}} = -\frac{v^*_B}{1-v^*_B}\left(\frac{1}{E^*_{eff}\big|_{Voigt}} + s^*_{12}\right)\cos^2(\theta)E^*_{XX}\bar{\epsilon}^*_{XX} \tag{20}$$

Eqs. (9)–(17) Liu et al. (2009) can be solved to find $\epsilon^*_{zz}|_{B,\bar{\sigma}^*_{zz}}$

$$\epsilon^*_{zz}|_{B,\bar{\sigma}^*_{zz}} = \left[\frac{(1+v^*_B)(1-2v^*_B)}{1-v^*_B}\frac{1}{E^*_B} - \frac{2v^*_B}{1-v^*_B}s^*_{13}\right]\sin^2(\theta)E^*_{XX}\bar{\epsilon}^*_{XX} \tag{21}$$

The magnitudes of the normal strains in the polymer, normalized to the magnitude of the macroscopic normal strain, $|\bar{\epsilon}^*_{XX}|$, are shown as a function of Φ_A in Fig. 4a–c. While the *zz* component is much higher than $|\bar{\epsilon}^*_{XX}|$ for $\theta = 10°$, 45° and 90° at high values of Φ_A, the *xx* component is less than $|\bar{\epsilon}^*_{XX}|$ except for $\theta = 0°$ (then it is equal to $|\bar{\epsilon}^*_{XX}|$) and the *yy* component is always lower than $|\bar{\epsilon}^*_{XX}|$.

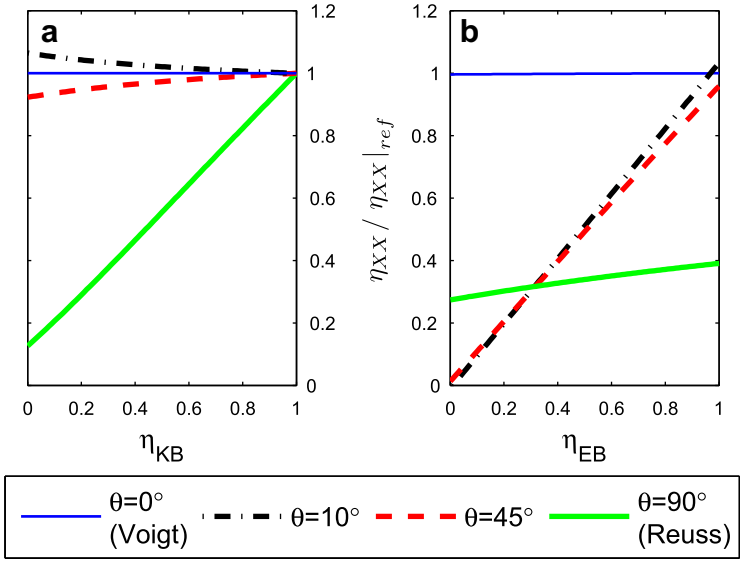

Fig. 3. Effective loss factor of layered composites, η_{XX}, as a function of the bulk loss factor of material B, η_{K_B} a., and of the tensile loss factor of material B, η_{E_B} b. Φ_A is set to 95%. The loss factors are normalized to the loss factor obtained when $\eta_{K_B} = \eta_{E_B} = 1.0$.

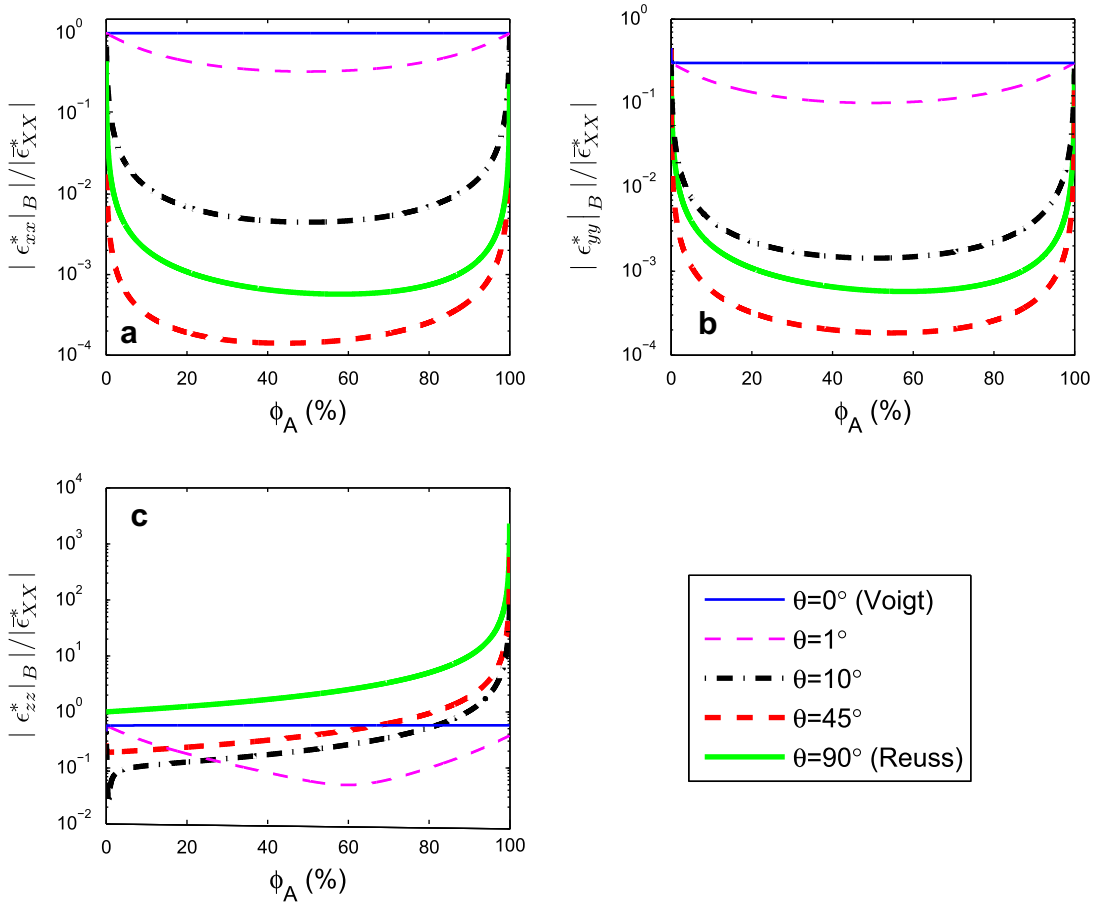

Fig. 4. Magnitude of the normal strains in the polymer as a function of Φ_A. a. *xx* component. b. *yy* component. c. *zz* component. All values are normalized to the magnitude of the macroscopic normal strain, $|\bar{\epsilon}^*_{XX}|$.

3.2. Shear strains

The *xy* and *yz* components of strains in the polymer are 0. The *xz* shear stress component in material B, $\tau^*_{xz}|_B$, is the same as the *xz* component of the macroscopic stress, $\bar{\tau}^*_{xz}$. so that

$$\gamma^*_{xz}|_B = \frac{\sin\theta\cos\theta}{G^*_B} E^*_{XX} \bar{\epsilon}^*_{XX} \tag{22}$$

The magnitude of $\gamma^*_{xz}|_B$ normalized to the magnitude of $\bar{\epsilon}^*_{XX}$ is shown as a function of Φ_A in Fig. 5. For the Voigt ($\theta = 0°$) and the Reuss

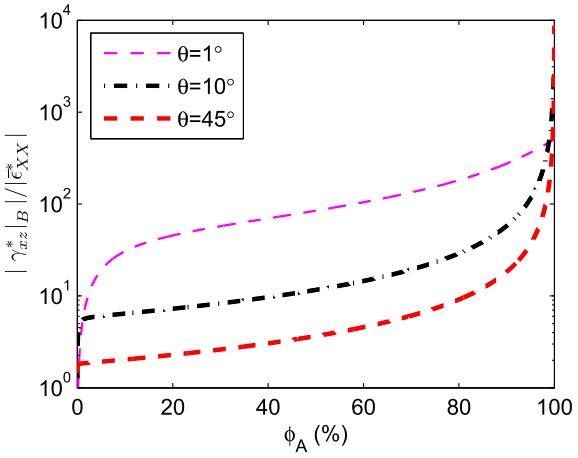

Fig. 5. Magnitude of the shear strain in the polymer, $|\gamma^*_{xz}|_B|$, normalized to the magnitude of the macroscopic normal strain, $|\bar{\epsilon}^*_{XX}|$, as a function of Φ_A.

($\theta = 90°$) topologies, the *xz* shear component is 0. In other cases, the normalized magnitude of $\gamma^*_{xz}|_B$ is very high at high volume fractions.

3.3. Equivalent strains

The time dependent strain components, $\epsilon_{(ij)}(t)$ (where $i,j = 1,3$) can be expressed as a function of the magnitude and phase of the complex-valued strain components. A time-dependent equivalent strain measure, $\epsilon_{eq}(t)$, can be computed using these time dependent values:

$$\epsilon_{eq}(t) = \sum_{ij} \frac{2}{3}\left[\epsilon^{dev}_{(ij)}(t)\right]^2 \tag{23}$$

where

$$[\epsilon_{\mathbf{dev}}](t) = [\epsilon(t)] - \frac{1}{3} tr[\epsilon(t)]\mathbf{I} \tag{24}$$

where $\mathbf{I}$ is the identity matrix and *tr* is the trace operator. The maximum value of $\epsilon^B_{eq}(t)$, $\epsilon^B_{eq}\big|_{max}$, normalized to the magnitude of $\bar{\epsilon}^*_{XX}$, is shown as a function of Φ_A in Fig. 6. The equivalent strain in material B is much higher than the macroscopic strain at high volume fractions, except in the case of the Voigt topology. Therefore simultaneous high levels of damping and stiffness are obtained due to a large equivalent strain in material B.

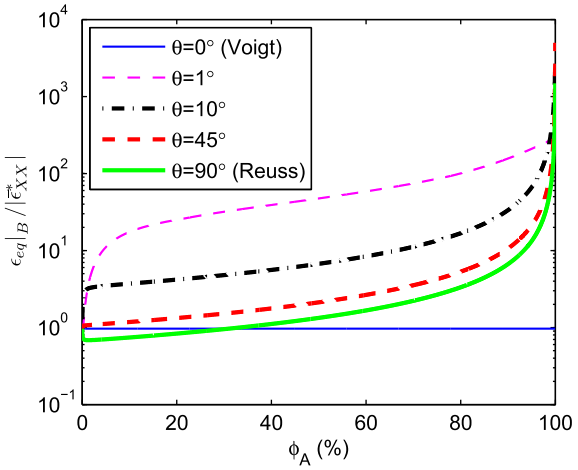

Fig. 6. Magnitude of the equivalent strain in the polymer, $\epsilon^B_{eq}\big|_{max}$, normalized to the magnitude of the macroscopic normal strain, $|\bar{\epsilon}^*_{XX}|$, as a function of Φ_A.

4. Optimal design

4.1. Optimization problems

Our objective is to design materials with both high stiffness and damping at small macroscopic strain amplitude. For this multiobjective optimization problem, we chose to minimize the following objective function:

$$f(\theta,\Phi_A) = \alpha \times \frac{|E^*_{ref}|}{|E^*_{XX}|} + (1-\alpha)\times\frac{\eta_{ref}}{\eta_{XX}} \tag{25}$$

where α is a weighting factor between 0 and 1. We chose to set $|E^*_{ref}|$ to the dynamic modulus of material A (200 GPa) and η_{ref} to the tensile loss factor of material B (1.0).

The results of the previous section show that high levels of stiffness and damping are due to very large strains in material B. However, lossy polymers tend to exhibit significant nonlinearity even at moderate strains (starting from a few percents). Moreover the presence of large strains in the polymer could cause failure of the composites even at small macroscopic strains. Therefore we constrain the ratio of the equivalent strain in the polymer to be less than 25 times the macroscopic normal strains $|\epsilon^*_{XX}|$. This maximum allowable strain is somewhat arbitrary but does enable the effect of strain constraints to be observed on the optimal properties and optimal configuration of the designed composites. The constrained optimization problem is given below:

$$\begin{aligned} &\underset{\theta,\Phi_A}{\text{minimize}} \quad f(\theta,\Phi_A) \\ &\text{subject to} \quad \frac{\epsilon_{eq}}{|\bar{\epsilon}^*_{XX}|} \leqslant 25 \end{aligned}$$

We use the Matlab function *fmincon* for constrained nonlinear optimization employing the SQP algorithm. We considered the same material A as in previous sections and two different materials for material B:

1. Polymer 1: $|E^*| = 20$ MPa, $\eta_E = 1.0$ (same as in previous sections).
2. Polymer 2: $|E^*| = 100$ MPa, $\eta_E = 1.0$.

4.2. Optimization results

Optimization was performed both without the constraint and with the constraint. The weighting factor, α, was varied from 10^{-5} to $1-10^{-5}$ to generate a line in the stiffness-loss map, also known as the Pareto front, such that there exists no feasible solution using layered composites with simultaneously higher dynamic modulus and loss factor than any point of the generated line. The Pareto fronts are shown in Fig. 7 for the two polymers considered for this study. In contrast to Fig. 2d, neither θ nor ϕ_A are constant on the Pareto fronts, as each point on the line corresponds to the optimal values of θ and ϕ_A for a specific value of α.

The stiffness-loss maps obtained for the unconstrained optimization with polymers 1 and 2 are approximately the same (the green[1] lines in Fig. 7). This implies that the stiffness of the lossy material has a minimal influence on the optimal stiffness and damping of the composite. The constraint on the strains in the polymer has a significant effect on the Pareto fronts (shown in the red dashed lines in Fig. 7), particularly with the softer polymer (polymer 1). It affects the stiffness-loss map except at very small values of α. Comparing the stiffness-loss maps for the constrained optimization with polymers 1 and 2 reveals that polymer 2 is a better choice than polymer 1 for designing composites with both high stiffness and

[1] For interpretation of color in Fig. 7, the reader is referred to the web version of this article.

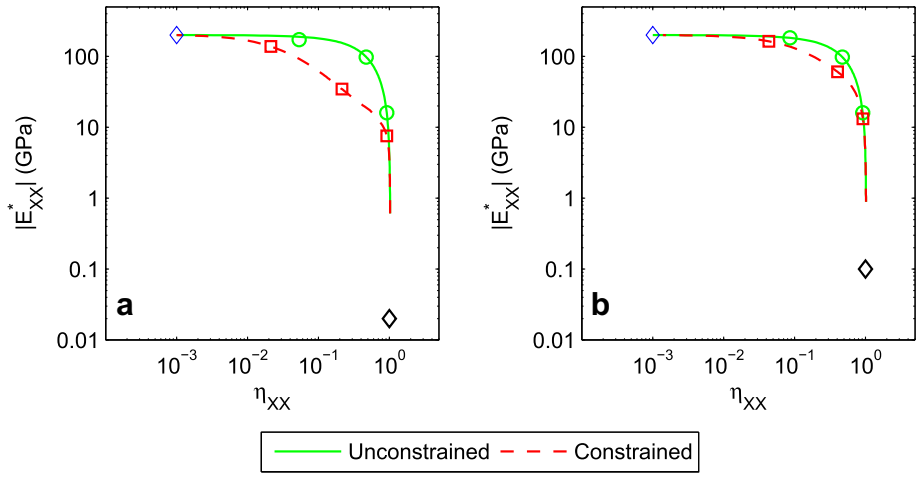

Fig. 7. Stiffness-loss map of the optimal unconstrained and constrained solutions, for α varying from 10^{-5} to $1-10^{-5}$. a. With polymer 1. b. With polymer 2. The circles (respectively squares) correspond to the optimal unconstrained (respectively constrained) solution for $\alpha = 0.01$, 0.5 and 0.99. The diamonds correspond to material A and material B.

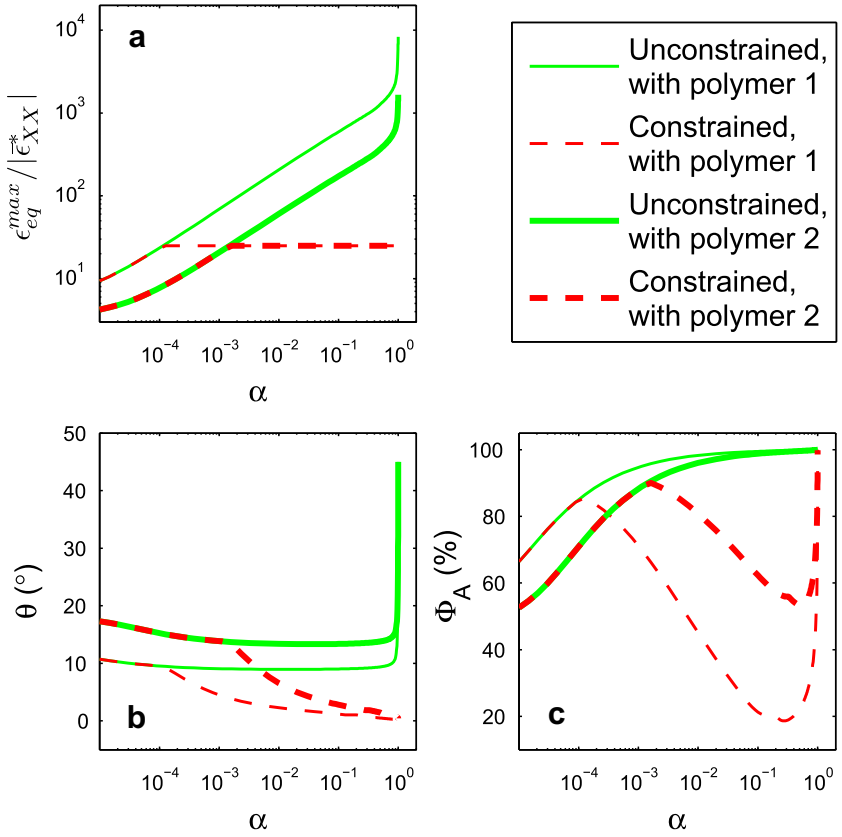

Fig. 8. a. Equivalent value of the strains in the polymer, ϵ_{eq}^{max}, normalized to the magnitude of the macroscopic normal strain, $|\bar{\epsilon}^*_{XX}|$. b. Optimal value of θ. c. Optimal value of Φ_A.

high damping if the strains in the polymer are constrained.

The equivalent strain in the polymer, ϵ_{eq}^{max}, normalized to the magnitude of the normal macroscopic strain, $|\bar{\epsilon}^*_{XX}|$, is plotted as a function of α in Fig. 8a. For the unconstrained optimization, the strains in the polymer increase monotonically with α and are larger in polymer 1 than in polymer 2. Therefore the constraint is active at lower values of α with polymer 1 than polymer 2. Even though the Pareto fronts obtained for the unconstrained optimization are almost indistinguishable between polymers 1 and 2, the optimal values of θ and Φ_A are significantly different (see Fig. 8b and c). With the softer polymer (polymer 1), lower values of θ and larger values of Φ_A are required. Moreover, the constraint reduces the optimal value of θ (almost 0 ° in the case of polymer 1) and reduces the optimal value of Φ_A (except for $\alpha \approx 1$). The optimal value of θ decreases monotonically with α and the optimal value of Φ_A increases monotonically with α in the case of the unconstrained optimization. In the case of the constrained optimization, an increase in α (increasing the weighting on the stiffness) requires simultaneous decreases in θ and Φ_A for $\alpha \leqslant 0.2$. This result is unexpected as it means that obtaining a stiffer composite requires a lower vol-

Table 1
Optimal solution for $\alpha = 0.5$.

Polymer	1	1	2	2
Constraint	No	Yes	No	Yes
$\lvert E^*_{XX}\rvert$ (GPa)	97.9	34.6	97.8	60.6
η_{XX}	0.474	0.215	0.472	0.404
Φ_A (%)	99.8	22.3	99.6	53.4
θ (°)	9.37	0.527	13.8	1.44
$\epsilon^B_{eq}\big\rvert_{max}/\lvert\epsilon^*_{ZZ}\rvert$	1270	25	366	25

Table 2
Material parameters for polyurethane.

Parameters	Value
μ	1.0810 MPa
λ_m	4.47
ν_0	0.48
G_1	4.04 MPa
K_1	6.73 MPa
τ_1	1.21 s
G_2	15.0 MPa
K_2	25.1 MPa
τ_2	0.163 s
G_3	1.85 MPa
K_3	3.09 MPa
τ_3	23.0 s
G_4	107 MPa
K_4	179 MPa
τ_4	0.0023 s
G_5	43.3 MPa
K_5	72.1 MPa
τ_5	0.0225 s

ume fraction of the stiff constituent. The optimal dynamic modulus, loss factor and design variables obtained for $\alpha = 0.5$ are shown in Table 1. Note that the constrained optimal composite with polymer 2 has almost the same dynamic modulus as aluminium and a loss factor of 0.4.

5. Dependence of the effective properties on the strain amplitude and frequency

The results of the optimization have demonstrated that combination of high stiffness and high damping are obtained when strains in the polymer are much higher than the macroscopic normal strains. Moreover, the composites exhibit significant axial-shear coupling and the resulting macroscopic shear strains can be much higher than the macroscopic normal strain when θ is close to 0. While we are interested here in the stiffness and damping at low macroscopic normal strains, high strains in the polymer or high macroscopic shear strains could affect the stiffness and damping due to geometric and/or material nonlinearity even when the macroscopic normal strain is low. Using finite deformation models, we simulate the response of layered composites with the geometrical parameters corresponding to configurations on the Pareto fronts obtained with the linear viscoelastic model.

5.1. Finite strain viscoelastic model

The polymer was modeled using a time-domain finite strain viscoelastic model. The rate dependent behavior was modeled using Prony series, and the rate independent high stretchability using a compressible hyperelastic Arruda and Boyce model (1993). The parameters (listed in Table 2) were determined using the procedure described in Sain et al. (in preparation) to fit, using a single set of parameters, an extensive set of data for a high loss polyurethane manufactured by our collaborators at the University of Michigan. The model simulations for the pure polymer agree well with DMA data over a wide frequency range (from 0.1 to 100Hz), uniaxial loading/unloading tensile measurements up at various constant strain rates (from 0.5%/s to 10%/s) and strain amplitude (from 0.5% to 10%) and relaxation tests. Simulations of the response of the composites to a sinusoidal strain input were run in Abaqus/Standard using an implicit algorithm. Generalized plane strain bilinear quadrilateral elements (CPEG4) were employed, as it allows the elements to have the same non-zero out-of-plane strain, which corresponds to the assumption of the Eq. (15) for composites with infinite out-of-plane dimensions. A representative finite element mesh for a unit cell of height H and width W is shown in Fig. 9. Since the strains are uniform in each phase, a coarse mesh is sufficient. Periodic boundary conditions were applied between nodes on opposite edges of the unit cell. The following constraints equations were applied between nodes of coordinates $(X_i, Z_i + W)$ (on the right edge) and (X_i, Z_i) (on the left edge):

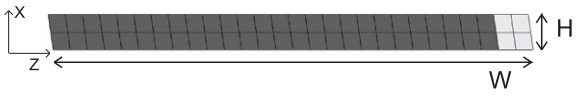

Fig. 9. Representative finite element model for a unit cell of height H and width W.

$$U_X(X_i, Z_i + W)(t) - U_X(X_i, Z_i)(t) = 0 \tag{26}$$

$$U_Z(X_i, Z_i + W)(t) - U_Z(X_i, Z_i)(t) = U_Z|_{ref}(t) \tag{27}$$

The following constraint equations were applied between nodes of coordinates $(0, Z_i)$ (on the bottom edge) and $(H, Z_i - Hsin\theta)$ (on the top edge)

$$U_X(H, Z_i - Hsin\theta)(t) - U_X(0, Z_i)(t) = U_X|_{ref}(t) \tag{28}$$

$$U_Z(H, Z_i - Hsin\theta)(t) - U_Z(0, Z_i)(t) = 0 \tag{29}$$

where $U_X|_{ref}(t)$ and $U_Z|_{ref}(t)$ denote the X and Z displacements of a reference node. $U_X|_{ref}(t)$ was prescribed to vary as a sinusoidal function of time. In order to eliminate rigid body motion, the X and Z components of the bottom left corner were sets to 0 and the X component of the bottom right corner was set to 0. The macroscopic normal stress, $\bar{\sigma}_{XX}(t)$, is given by:

$$\bar{\sigma}_{XX}(t) = \frac{R_X|_{ref}(t)}{U_X|_{ref}(t)} \frac{H}{W} \tag{30}$$

where $R_X|_{ref}$ is the reaction per unit length measured at the reference node. Eq. (3) cannot be used to compute the loss factor in the case of a nonlinear material response. However, an energy-based definition of damping can be used. In a linear viscoelastic material (Lakes, 2009), the loss factor is equal to:

$$\eta_{XX} = \frac{W_d}{W_s} \tag{31}$$

where W_d is the energy dissipated per cycle during sinusoidal loading, which is equal to the area within the stress/strain hysteresis loop. W_s, the stored energy is equal to the area of the triangle connecting the origin, the point with maximum strain, and the projection of this point onto the horizontal axis. Eq. (31) can be generalized to define the loss factor of a nonlinear material. Due to nonlinearity, the stored energy in compression and in tension might be different. In order to take into account the full cycle, we chose to define the stored energy as the average of the stored energy in compression and in tension. Similarly we defined the storage modulus as the average of the absolute values of the slopes connecting the origin with the point with maximum strain and to the point with minimum strain. The 3rd cycle was chosen for the

computations since transient effects have almost vanished after 2 cycles.

In order to compare simulations with the theoretical formulae derived in this paper, we computed the effective modulus using Eq. (15) with a linear viscoelastic model equivalent to the nonlinear model at infinitesimal strains. At infinitesimal strains, the frequency-dependent shear modulus, $G^*(\omega)$, and bulk modulus, $K^*(\omega)$, are given by:

$$G^*(\omega) = G_0 + \sum_{j=1}^{N_b} \frac{G_j i\omega\tau_j}{1+(\omega\tau_j)^2} \tag{32}$$

$$K^*(\omega) = \sum_{j=1}^{N_b} \frac{K_j i\omega\tau_j}{1+(\omega\tau_j)^2} \tag{33}$$

where G_0 (respectively K_0) is the long term shear modulus at infinitesimal strains (respectively long term bulk modulus at infinitesimal strains), N_b is the number of terms in the Prony series. Eq. (15) requires the value of the complex Young's modulus, $E^*(\omega)$, and complex Poisson's ratio, $v^*(\omega)$, which are given by:

$$E^*(\omega) = \frac{9K^*(\omega)G^*(\omega)}{3K^*(\omega)+G^*(\omega)} \tag{34}$$

$$v^*(\omega) = \frac{3K^*(\omega)-2G^*(\omega)}{6K^*(\omega)+2G^*(\omega)} \tag{35}$$

5.2. Comparison between linear and nonlinear model

The optimization for the effective dynamic modulus and loss factor at 1 Hz was carried out using the linear viscoelastic model. Predictions for the effective dynamic modulus and loss factor using the finite strain model are compared to the results obtained with the linear viscoelastic model, using the same geometrical parameters, for different values of the macroscopic strain amplitudes (between 0.01% and 1%) of frequency 1 Hz in Fig. 10. As expected, both for the unconstrained optimization and for the constrained optimization, the nonlinear simulations converge toward the linear viscoelastic theory as the strain amplitude is reduced. In the case of the unconstrained optimization, the nonlinear simulations start to differ significantly (by more than 25%) from the linear results when the macroscopic strain amplitude is higher than 0.8% (in the case of $\alpha = 0.5$). Nonlinear effects play a bigger role in the case of the constrained optimization, since the strain amplitude needs to be less than about 0.02% to have effective properties within 25% of the linear viscoelastic theory in the case of the stiffest configuration (obtained with $\alpha = 0.9$).

Comparisons between the predictions for the macroscopic normal stress, $\bar{\sigma}_{XX}(t)$, between the linear viscoelastic model and the finite deformation model are shown in Fig. 11 for the unconstrained optimization, for a strain amplitude of 0.1%. Despite the high strains in the polymer, the two models predict almost exactly the same macroscopic strain. However, in the case of the constrained optimization (shown in Fig. 12), there are some significant differences. The nonlinear model predicts a lower stiffness and higher damping in compression than the linear viscoelastic model. The opposite trend is observed in tension. The constrained optimal solution tends to have a much smaller value of θ than the unconstrained optimal solution (Fig. 8b). While these configurations with low values of θ have high stiffness at infinitesimal strains, an axial load tends to cause a large shear deformation, causing θ to increase under compression. Moreover, at low values of θ, the effective stiffness is extremely sensitive to the value of θ. Therefore compression causes a softening and an increase in damping.

5.3. Frequency dependence

The results predicted by Eq. (15) at for frequencies between 0.1 and 100 Hz are plotted in a stiffness-loss map in Fig. 13 for the unconstrained optimal configurations for different values of α. Interestingly, the polymer as well as the $\alpha = 0.001$ configuration

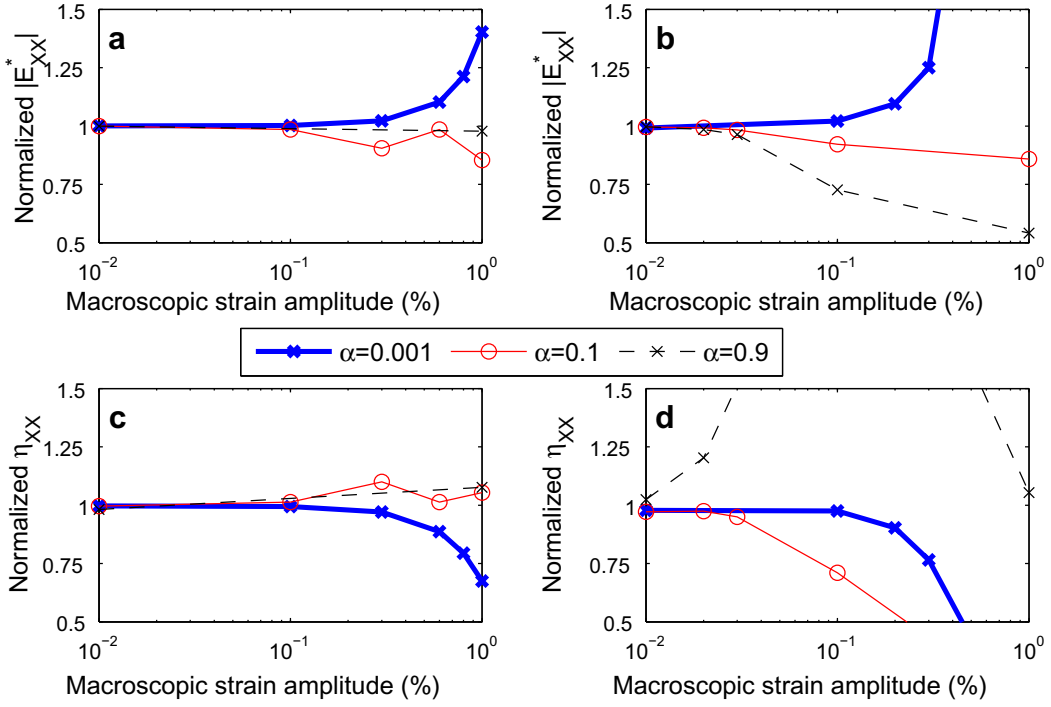

Fig. 10. Dependence of the effective dynamic modulus, a. and b. and loss factor, b. and d. on the macroscopic strain amplitude. All properties are normalized by the values predicted by the linear viscoelastic model. a. and c. correspond to the configurations obtained with the unconstrained optimization. b. and d. correspond to the configurations obtained with the constrained optimization.

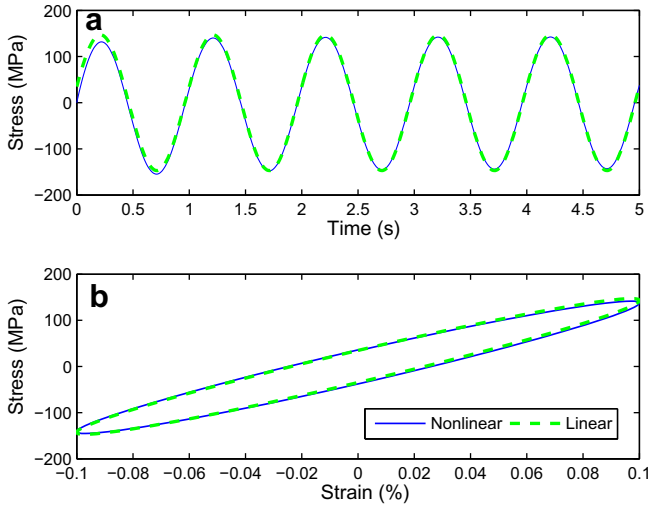

Fig. 11. Comparison between linear viscoelastic model and finite deformation model, for the geometric parameters corresponding to the unconstrained optimization with $\alpha = 0.5$. a. Stress as a function of time. b. Stress as a function of strain, during the 3rd cycle.

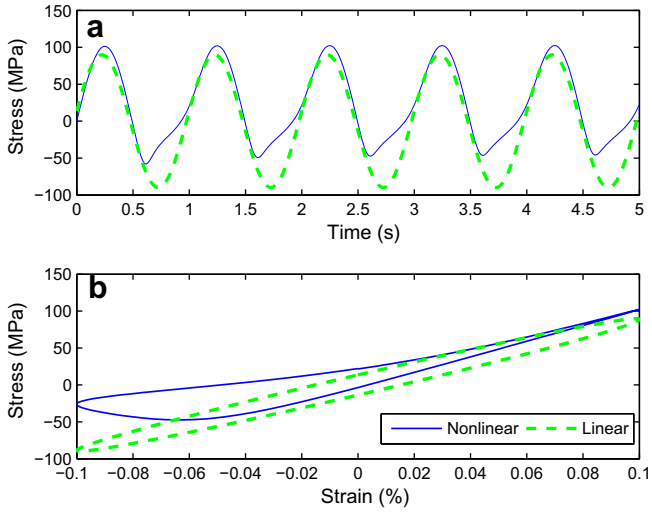

Fig. 12. Comparison between linear viscoelastic model and finite deformation model, for the geometric parameters corresponding to the optimization with $\alpha = 0.5$ when the maximum allowable strain in the polymer is constrained to be less than 25 times $|\bar{\epsilon}^*_{XX}|$. a. Stress as a function of time. b. Stress as a function of strain, during the 3rd cycle.

have a stiffness that is very sensitive to the frequency (varying by more than one order of magnitude between 0.1 and 100 Hz). The configuration using $\alpha = 0.99$ has a loss factor that depends strongly on frequency, while the stiffness is approximately independent of frequency.

6. Effects of finite size and boundary conditions

The above analysis and optimization of layered composites of infinite size demonstrated that a layered composite can have extremely high stiffness and damping. However physical composites have a finite size. Therefore it is important to determine the minimum size required to approach the results derived in the previous sections. Here we investigate using a linear viscoelastic model the

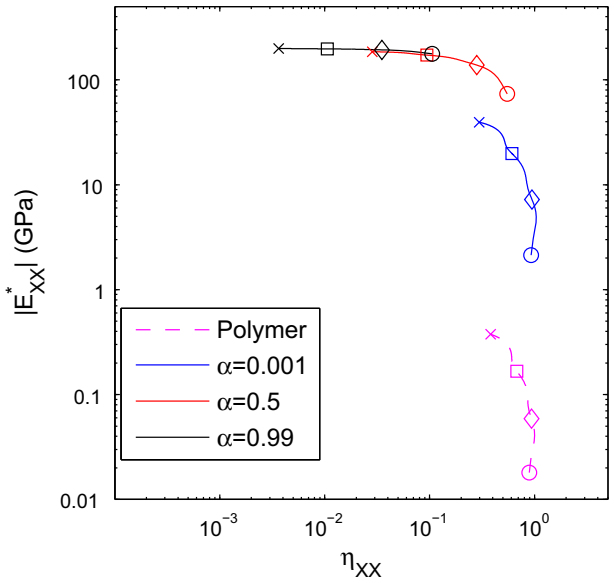

Fig. 13. Stiffness-loss map of the frequency-dependent properties obtained for the optimal unconstrained optimization with $\alpha = 0.001$, 0.5 and 0.99. The circles correspond to the value at 0.1 Hz; the diamonds to the values at 1 Hz; squares to the values at 10 Hz; the crosses to the values at 100 Hz.

dependence of the effective dynamic modulus and loss factor on size for composites with the optimal unconstrained geometry.

6.1. Numerical model

Abaqus (2011) was used to simulate the response of layered composites of finite sizes to a harmonic load of frequency 1 Hz. We use frequency domain linear viscoelastic models using the Prony series coefficient of Table 2. Generalized plane strain bilinear quadrilateral elements (CPEG4) were employed. We considered

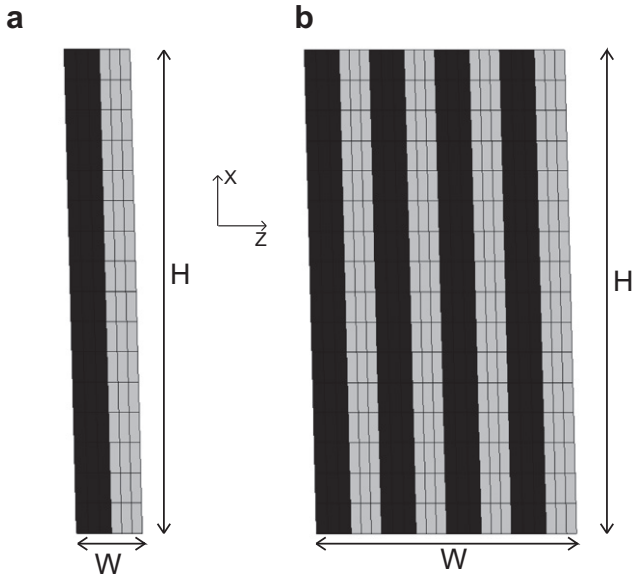

Fig. 14. Examples of models used to determine the effect of the finite size on the effective dynamic properties of layered composites. For both models shown here, $\frac{H}{T_B} = 50$, $\theta = 88.56°$ and $\phi_A = 53.4\%$. a. Unit cell of the model with finite height. b. Model with finite height and finite number of layers (4 layers each of material A and material B, $N_{layer} = 4$).

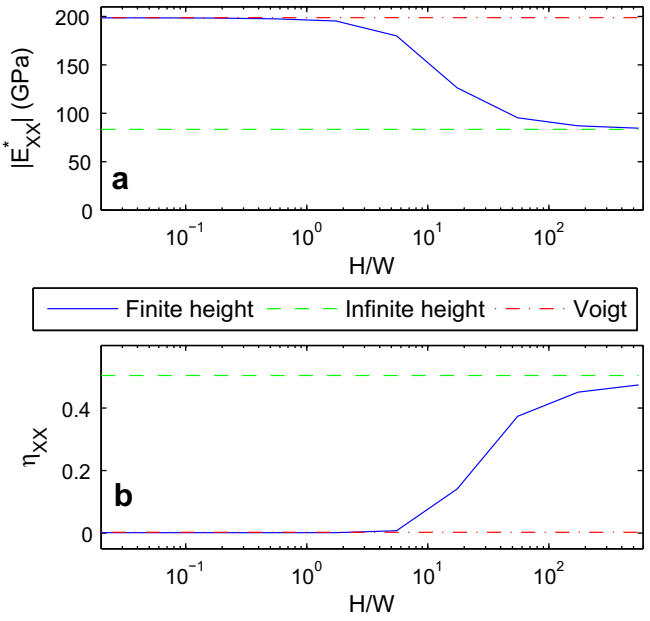

Fig. 15. Effect of the ratio $\frac{H}{W}$ on the effective dynamic modulus, $|E^*_{XX}|$ a., and effective loss factor, η_{XX} b., of composites with infinite number of layers.

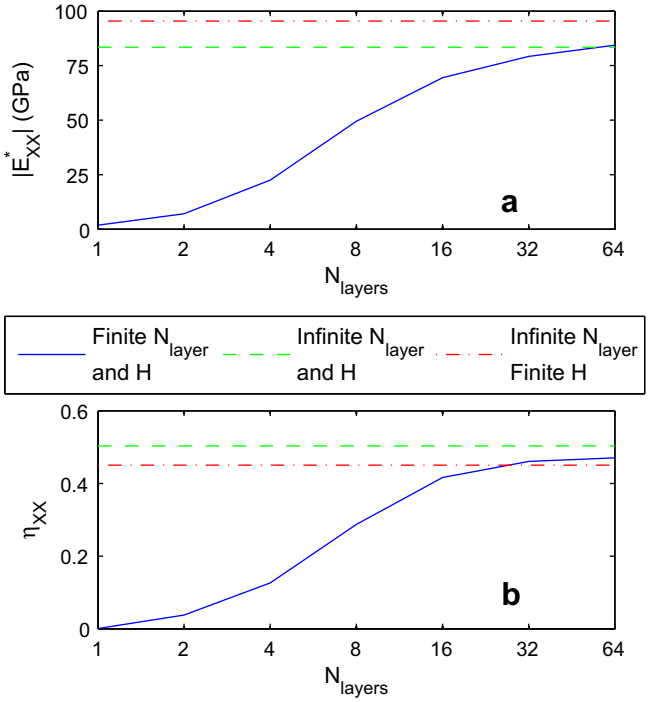

Fig. 16. Effect of the number of layers on the effective dynamic modulus, $|E^*_{XX}|$ a., and effective loss factor, η_{XX} b., of composites with finite height.

composites with a finite height, H, and an infinite number of layers, and composites with a finite height, H, and a finite number of layers, N_{layer}. In both cases, a harmonic vertical displacement, U_0, is applied to the top edge and the vertical displacement of the bottom edge and the horizontal displacement of the bottom right corner are set to zero.

For a composite of finite height and infinite number of layers, we modeled a unit cell of width W and height H (see Fig. 14a, for a representative model). Periodic boundary conditions were applied on the left and right edges, resulting in constraint equations between each node of coordinate (X_i, Z_i) of the left boundary and of coordinate $(X_i, Z_i + W)$ of the right boundary:

$$U_X(X_i, Z_i + W) - U_X(X_i, Z_i) = 0 \tag{36}$$

$$U_Z(X_i, Z_i + W) - U_Z(X_i, Z_i) = U_Z|_{ref} \tag{37}$$

where $Z_i = -X_i \times \tan\theta$ and $U_Z|_{ref}$ is the horizontal displacement of a reference node. Fig. 14b shows one example finite element model for the case of a composite of finite height and finite number of layers. The left and right edges of the finite layer composite are unconstrained. In both cases, the effective complex Young's modulus is given by:

$$E^*_{XX} = \frac{H}{W}\frac{R^*_X}{U_0} \tag{38}$$

where R^*_X is the reaction force per unit length on the bottom edge (Sun and Vaidya, 1996).

6.2. Effect of a finite height of the effective dynamic properties

The effective dynamic modulus, $|E^*_{XX}|$, and loss factor, η_{XX}, are plotted as a function of the ratio of the height of the composites to the width of the composites, $\frac{H}{W}$, in Fig. 15a and b. As $\frac{H}{W}$ is increased, $|E^*_{XX}|$ decreases and η_{XX} increases. We observed the opposite trend for cylindrical Reuss composite rods of finite radius (Meaud and Hulbert, in press). At low values of the ratio $\frac{H}{W}$, the strains in material A and B are identical and therefore, the effective properties are approximately given by the Voigt formula $(E^*_{XX} = \Phi_A E^*_A + (1 - \Phi_A)E^*_B)$ which makes the dynamic modulus much higher and the loss factor much lower than predicted by Eq. (15). Higher values of $\frac{H}{W}$ are necessary for the polymer layers to deform in shear. At high values of the ratio $\frac{H}{W}$, the effective properties approach the values given by Eq. (15), which validates the derivations of this paper. The height, H, needs to be more than 100 times the width, W, to have properties within 10% of the values given by Eq. (15).

6.3. Effect of a finite number of layers on the effective dynamic properties

Based on the results discussed above, the ratio of the height to the thickness of the layers of material B was chosen to be 130 for composites of finite height and finite number of layers. The effective dynamic modulus and loss factor are plotted as a function of the number of layers, N_{layer}, in Fig. 16a and b. The effective dynamic modulus and the loss factor of the composites tend to increase as the number of layers is increased. When the number of layers is small, the layers of material A carry almost exclusively the load and therefore the damping is small. Moreover when N_{layer} is low, the vertical load, F^*_{XX}, causes a nonnegligible shear stress, $\bar{\tau}^*_{XZ}$ (because of the geometry of the composite), which reduces the effective stiffness of the composite. As the number of layers is increased, material B contributes more to the stiffness of the composite because the deformation of the material is more constrained and the macroscopic shear stress becomes negligible. The change in the mode of deformation of the composite induces shear dissipation in material B. Approximately 64 layers are needed to approximate the effective properties of the composite of infinite size.

7. Conclusions

In this paper we investigated the effective dynamic modulus and loss factor of layered composites with parallel plane layers loaded in an arbitrary direction. We derived formulae for composites of infinite dimensions and analyzed the dependence of the

effective properties on the volume fractions and angle as well as on the bulk and tensile loss factors of the lossy constituent. We also derived the magnitude of the strains in the polymer and showed that the combination of high stiffness and high loss factor is due to the nonaffine deformation. Further we optimized the geometrical parameters of these composites both without and with a constraint on the strains in the polymer to be of moderate magnitude. Composites with high stiffness and high damping were obtained. As expected, simulations using finite deformation models converge to the linear viscoelastic model at low macroscopic strain amplitude. In the case of the unconstrained optimization, the finite deformation and linear viscoelastic models agree well for strains amplitudes up to a few tenths of a percent despite the presence of very high strains in the polymer. Deviations from the linear viscoelastic theory are observed at lower macroscopic strain amplitudes in the case of the constrained optimization. The behavior of these configurations is due the softening in compression and stiffening in tension induced by nonlinear geometric effects. In future studies, these nonlinear geometric effects could be potentially exploited to design adaptive materials that respond differently depending on the magnitude of the loads. The use of wavy layers to selectively induce nonlinear geometric effects that are different in tension and compression has been studied by us as reported in Sain et al. (in press). We also considered the practical considerations of the finite size of manufacturable composites. Because the effective properties are highly dependent on the height of the composites and on the number of layers, we determined the minimum size required to attain comparable performance as the infinite dimensional case.

Acknowledgments

This work has been supported by the Defense Advanced Research Projects Agency (DARPA) Strategic Technology Office, under program manager Dr. Aaron Lazarus. The authors thank Dr. Bongjun Yeom and Prof. Nicholas Kotov for manufacturing the polyurehane and Bret Kitcher and Prof. Ellen Arruda for measuring the mechanical properties of the polyurethane.

References

ABAQUS User Manual. Version 6.11, Hibbitt, Karlsson & Sorensen, Inc., 2011.

Arruda, E.M., Boyce, M.C., 1993. A three-dimensional constitutive model for the large stretch behavior of rubber elastic materials. Journal of the Mechanics and Physics of Solids 41, 389–412.

Ashby, M., 1989. Overview no. 80: on the engineering properties of materials. Acta Metallurgica 37, 1273–1293.

Brodt, M., Lakes, R.S., 1995. Composite materials which exhibit high stiffness and high viscoelastic damping. Journal of Composite Materials 29, 1823–1833.

Cadman, J., Zhou, S., Chen, Y., Li, Q., 2012. On design of multi-functional microstructural materials. Journal of Materials Science, 1–16.

Chen, C.P., Lakes, R.S., 1993. Analysis of high-loss viscoelastic composites. Journal of Materials Science 28, 4299–4304.

Christensen, R., 2003. Theory of Viscoelasticity, second ed. Dover.

Guest, J.K., Prevost, J.H., 2006. Optimizing multifunctional materials: design of microstructures for maximized stiffness and fluid permeability. International Journal of Solids and Structures 43, 7028–7047.

Kim, H.J., Swan, C.C., Lakes, R.S., 2002. Computational studies on high-stiffness, high-damping SIC-INSN particulate reinforced composites. International Journal of Solids and Structures 39, 5799–5812.

de Kruijf, N., Zhou, S., Li, Q., Mai, Y.W., 2007. Topological design of structures and composite materials with multiobjectives. International Journal of Solids and Structures 44, 7092–7109.

Lakes, R., 2009. Viscoelastic Materials. Cambridge University Press.

Lakes, R.S., 2002. High damping composite materials: effect of structural hierarchy. Journal of Composite Materials 36, 287–297.

Liu, B., Feng, X., Zhang, S.M., 2009. The effective Young's modulus of composites beyond the Voigt estimation due to the Poisson effect. Composites Science and Technology 69, 2198–2204.

Meaud, J., Hulbert, G., in press. Dependence of the dynamic properties of Voigt and Reuss composites on the Poisson's ratio and bulk loss factor of the constituent materials. Journal of Composite Materials. doi: http://dx.doi.org/10.1177/0021998312463456.

Patel, R.K., Bhattacharya, B., Basu, S., 2007. A finite element based investigation on obtaining high material damping over a large frequency range in viscoelastic composites. Journal of Sound and Vibration 303, 753–766.

Prasad, J., Diaz, A., 2009. Viscoelastic material design with negative stiffness components using topology optimization. Structural and Multidisciplinary Optimization 38, 583–597.

Pritz, T., 2009. Relation of bulk to shear loss factor of solid viscoelastic materials. Journal of Sound and Vibration 324, 514–519.

Sain, T., Meaud, J., Hulbert, G., Arruda, E., Waas, A., in press. Simultaneous high stiffness and high damping in a class of wavy layered composites. Composite Structures.

Sain, T., Meaud, J., Kitcher, B., Waas, A., Arruda, E., in preparation. Rate dependent finite strain constitutive model for polymer-clay nanocomposites.

Sun, C., Vaidya, R., 1996. Prediction of composite properties from a representative volume element. Composites Science and Technology 56, 171–179.

Torquato, S., Hyun, S., Donev, A., 2002. Multifunctional composites: optimizing microstructures for simultaneous transport of heat and electricity. Physical Review Letters 89, 266601.

Yi, Y., Park, S., Youn, S., 2000. Design of microstructures of viscoelastic composites for optimal damping characteristics. International Journal of Solids and Structures 37, 4791–4810.